Unisanta Science and Technology, **2024, 1, September**
Published Online 2024 Vol.13 Nº2 http://periodicos.unisanta.br/index.php/sat)

UNISANTA
Science and Technology
ISSN 2317-1316

The Importance of Describing the Molten Pool to Understanding the Additive Manufacturing Process by Laser Powder Bed Fusion

Willy Ank de Morais [1,2], Fernando José Gomes Landgraf [2]

UNISANTA[1] – Universidade Santa Cecília – Faculdade de Engenharia – Graduação em Engenharia Mecânica
Rua Oswaldo Cruz, 266 - Santos-SP, Brasil - CEP: 11045-100

USP [2] – Departamento de Engenharia Metalúrgica e de Materiais – Escola Politécnica
Av. Professor Mello Moraes, 2463 - Butantã, São Paulo-SP, Brasil, CEP: 05508-030

E-mail*:* willyank@unisanta.br
Received August, 2024

Abstract: Additive manufacturing (AM) processes for metals do not have the same popularity as other materials due to development needs, innate safety concerns, and technological and operational costs. Among these, the laser powder bed fusion process (FLP-L) has stood out in recent years mainly due to its differential advantages. In this process, the dynamics of molten pool formation are decisive for the performance of an FLP-L product, including specific unique properties, such as its crystalline texture. Thus, molten pool formation, geometry, and overlaps are subjects of continued interest in the literature. Within this context, the present work reviews the literature on the main characteristics and conditions that control the formation and dynamics of molten pools, illustrating the information with records available in the literature, including those obtained from Nb-48Ti alloy powders. In conclusion, the work offers guidelines for establishing microstructural control conditions for a metallic product obtained by this process.

Keywords: Additive Manufacturing; Laser Powder Bed Fusion; LPBF; Molten Pool; Microstructural Control.

1. Introduction

The broader the possibilities for controlling structure in a manufacturing process, the easier it is to tailor properties to optimize the performance of engineering materials for a given application [1, 2]. This is precisely the great appeal of additive manufacturing (AM), whose various categories have great potential to obtain new forms of structure-properties-performance relationships, inducing technological innovations and new applications of engineering materials [3, 4]. Particularly for metals, the AM laser powder bed fusion (LPBF) process has been studied in this regard and with increasing interest due to its differential advantages over traditional production processes [5-7]:

(1) obtaining complex parts, allowing to implement topological optimization,
(2) minimum raw material requirement (metal powder),
(3) ability to work with high melting point metals and
(4) possibility of obtaining final parts without complex additional steps.

And the potential of control crystalline type and orientation (texture) [7-9].

As in other production processes, in LPBF, the structure formed and consequent product performance depends not only on the chemical composition of the powders used but especially on the processing conditions adopted [7-9]. In this sense, it is customary to define a "processing window" as the range of values in the production variables permissible to obtain a product that meets the requirements of its final use by AM [10, 11]. The size of the processing window, also known as 'printability' (or printability) [6, 9, 12], depends on the

Copyright © 2024 ISESC.

procedural conditions and the severity of the requirements necessary for the final application of the component, which can be geometric, physical, chemical and mechanical. To avoid complexity in considering the various performance variables that may be involved, the "processing window" is usually defined by the proximity of the specific mass ($\rho_{Product}$) obtained in the products to the monolithic density of the metal/alloy ($\rho_{Theoretical}$) or *%RD* [9, 13, 14], as defined by Eq. (1):

$$\%RD = \rho_{Product} / \rho_{Theoretical} \quad (1)$$

In addition to the various parameters of the LPBF process [15, 16], the most frequently reported in the available literature to define the "processing window" are the power (P), the scanning speed (v), linear energy (or thermal input) (E_L) and volumetric energy (E_V), the latter two described by Eq. (2) and Eq. (3):

$$E_L = P / v \quad (2)$$

$$E_V = 10^6 \cdot E_L / (\lambda \cdot h) = 10^6 \cdot P / (v \cdot \lambda \cdot h) \quad (3)$$

Where: P (W) is the power; v (mm/s) is the scan speed; λ (μm) is the lath distance or distance between laser scan passes; and h (μm) is the table lowering step, E_V (J/mm^3) the volumetric, and E_L (J/mm) linear energy.

During the LPBF process, the laser scans the deposited powder bed, fusing the particles in the part construction positions very quickly, covering the distance of a molten pool (100 to 1000 μm) in milliseconds [17]. In the same way, the formation and solidification of a molten pool is a process of rapid evolution. Its study is quite challenging since the phenomena of heating, melting, solidification, and cooling occur in a very localized way and involve high cooling rates ($\dot{T}$) and solidification (R), with temperature gradients (G) that are typically on the order of 10^6 K/m as according to Bontha et al. [8] and DebRoy et al. [9]. These conditions generally favor solidifying large and elongated columnar grains [8, 9]. However, different microstructures can be induced depending on processing parameters, such as scanning strategy and speed (v), laser power (P), and distance between passes (λ), among others. Rasch et al. [11] exemplify this condition by presenting different microstructural results obtained with similar and various combinations of R and G, as illustrated in Figure 1.a. This characteristic can be exploited to microstructurally customize a component for a specific application, providing it with different microstructures, as described in Figure 1.b.

Although the available literature describes general aspects [6, 9] and some essential details [5, 7] of the LPBF process, there is still much to investigate and understand the influence of the countless variables in this process [16, 19]. How the variables of the LPBF process affect the properties of the obtained products, including the crystalline texture, can ultimately be addressed by how they define the dynamics of the molten pool, its melting mode, the associated geometry, formation sequence, and 3D superposition [10, 11, 20-23].

Therefore, this review article aims to describe the main topics regarding the formation characteristics of molten pools in the LPBF process, linking these to procedural parameters, which can be defined to control the microstructural evolution and, consequently, the product's properties. Recent cases from the literature are presented, addressing the link between molten pool

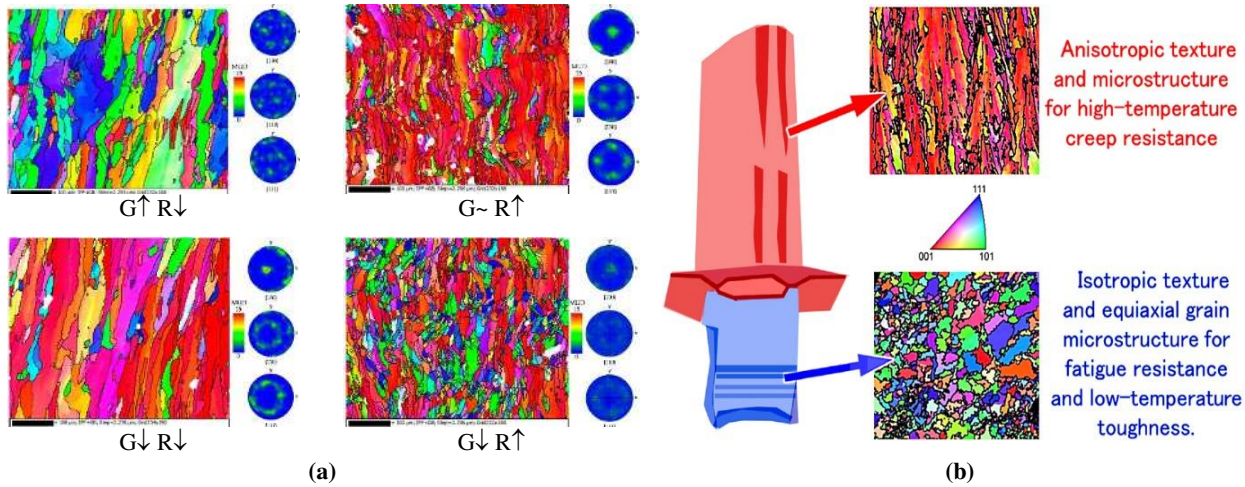

Figure 1. Example of microstructural variation in components produced by LPBF according to orientation maps obtained by EBSD: (a) influence of temperature gradients (G) and solidification rates (R) ranges in Al-Cu alloys [11] and (b) controlling of microstructures for aeronautical turbine blade [18].

Copyright © 2022 ISESC

dynamics and the properties of LPBF products. Finally, to exemplify some of the concepts described, laboratory data will be used from the case of an Nb-48Ti alloy, particularly described in another work submitted to this event.

2. Development

There are two basic modes in which molten pools can be formed in welding or AM processes, using energy beams: conduction and 'keyhole.' Figure 2 illustrates the differences between these modes, as described following:

- In conduction mode, the heat to create the molten pool in the material occurs by conduction from the surface, forming a molten pool of parabolic geometry in a cross-section and with d/w < 1.0 [23].
- In 'keyhole' mode, the molten pool formed is deeper, resembling a cross-section keyhole, and starts acting as a “black body” [25] that retains the beam's energy. This results in energy efficiency and very high peak temperatures that can even generate evaporation of the material being manufactured, with d/w > 1.5 [23].

In addition, a mixed mode can also be considered, in which the depth/width ratio (d/w ≈ 1) [23]. In LPBF, the prevalence of one mode or another will depend on the energetic conditions of the laser beam, as described by the basic parameters presented previously (P, v, and E_V).

In both melting modes, several phenomena associated with the formation of the molten pool occur, as illustrated schematically in Figure 3, in addition to simple melting and solidification, such as:

1. interaction between heat source and raw materials (powders),
2. heat and mass transfer and fluid flow,
   2.1. evaporation,
   2.2. convection (Marangoni flows),
   2.3. heat conduction,
   2.4. heat absorption/reflection by the puddle,
   2.5. spreading of fluid (spatter) or dust,
3. temperature and velocity distributions in the liquid,
4. puddle stability.

The description of the heat transfer between the laser, the molten pool, and the rest of the material needs to consider convective effects associated with events that occur in the molten pool and its surroundings, as illustrated in Fig. 3. Some simplifications are generally adopted: constant specific masses in the liquid and solid, flat deposited surfaces and neglecting the heat of vaporization of the alloying elements.

To address the conditions shown in Fig. 3, several works model the geometry and temperature distribution of the molten pool, which can be confirmed experimentally to calibrate and validate such models. This makes it possible to associate the production parameters adopted with the molten pools obtained and explain accessory phenomena. Some of these works consider the conduction mode and a symmetric parabolic geometry of the molten pool according to a plane perpendicular to the laser scanning direction [9, 27, 28]. The Rosenthal equation describes this geometry and is widely used in the simulation of welding processes [25] and used for LPBF process, as presented by Eq. (4):

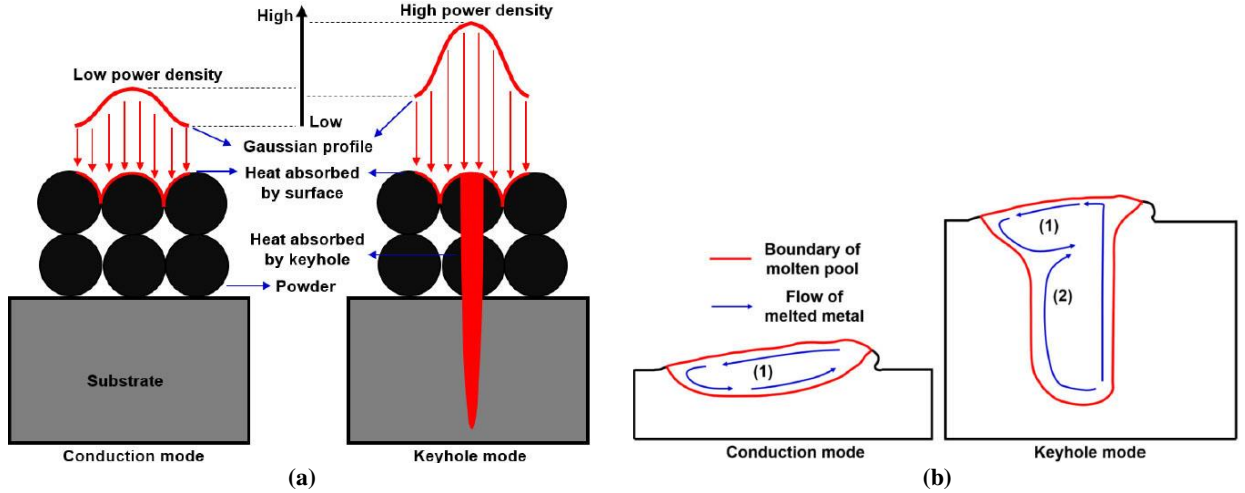

Figure 2. Illustrations of the two fusion modes that can be present in the LPBF process: (a) conduction and (b) 'keyhole' mode [24].

Copyright © 2022 ISESC

$$\frac{2\pi(T-T_0)kR}{Q} = exp\left[\frac{-v(R-x)}{2\alpha}\right] \quad (4)$$

Where: T is the temperature (K) considered and T_0 the temperature of the part before laser melting, respectively; k is the thermal conductivity of the part (W/(m·K)); R_d is the radial distance from the heat source (m); Q is the heat transferred from the heat source to the part (J); x is the coordinate (m); α is the thermal diffusivity that is equal to $k/(\rho \cdot C)$, where ρ and C are the density (kg/m^3) and the specific heat of the part (J/(Kg·K)), respectively.

materials with temperature and assumes a point source of heat rather than an actual Gaussian distribution of laser intensity. Furthermore, the effect of the spacing between scans (or tracks) horizontally and vertically (λ and h, respectively) is not considered, which will affect the temperature, overlap ($\%OvR$), profiles, and cooling rate, and, consequently, microstructural formation. Finally, the applicability condition of this equation is linked to the conduction melting mode, which is not always the best option to obtain a product with good relative density ($\%RD$) [17].

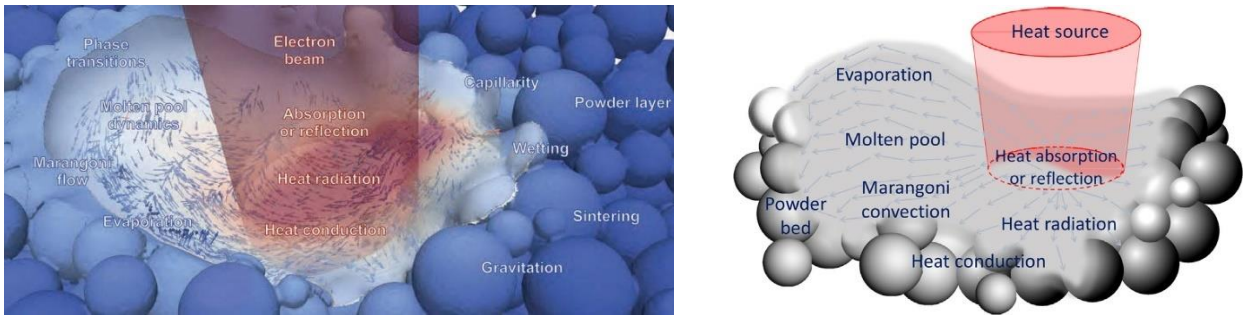

(a) **(b)**

Figure 3. General illustrations of the essential physical phenomena that occur during laser powder bed fusion by laser or electron bean: (a) more generally, including the movement within the molten pool represented by the arrows [26] and (b) focused on the molten pool [9].

From Eq. (4), a three-dimensional solution based on heat flow in a semi-infinite part can be derived to describe the typical geometry of a molten pool in LPBF. This type of geometry is used to study the phenomena of thermal exchanges throughout the deposited layers and to investigate the size and geometry (for example, lower concavity) of the molten pools generated by the process, as well as to couple Marongi liquid flow description models. as illustrated in Figure 4. Although Rosenthal's model is used in the literature, it is criticized due to the particularities of the LPBF process [29]. The model does not consider the change of thermophysical properties of

Transient 3D numerical models using finite element discretization are widely used to compensate for previously presented limitations [9]. Such models generate results such as those illustrated in Fig. 4, which revealed the relationship between the laser energy and the maximum temperature of the molten pool, the deformations, and the residual stresses present [19, 30]. Some studies simulate the entire process, from laser heating to material melting, to evaluate the impact of surface tension on the fluid flow in the molten pool, as shown in Fig. 4.b.

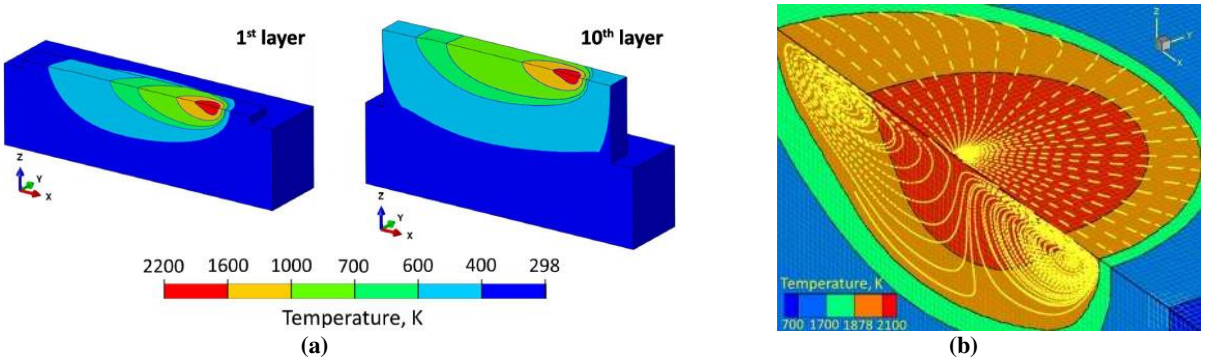

(a) **(b)**

Figure 4. Computational simulations of the IN 178 nickel alloy molten pool produced by LPBF illustrate the distribution of (a) the temperatures in the 1st and 10th layers [30] and (b) the circulation of molten metal driven by the surface tension gradient [9].

Copyright © 2022 ISESC

2.1. Quantifying the Size of Molten Pools and Their Mode of Formation

Several experimental works investigate the geometry of the molten pool considering a single track. This simplifies the analysis conditions because the already formed lateral scans are not present, with different thermal conductivity characteristics than the powder yet to be melted [31]. Through the metallographic analysis of the molten pools formed by single tracks, as illustrated in Figure 5.a, it becomes possible to evaluate the total melted area, the contact angle, and the width of the contact zone as a function of different parameter processes [6, 23].

In Fig. 5.a, it is possible to see the relationship between the production parameters (P and v) and the current melting mode, as illustrated in Figs. 2.a and 2.b. The conduction mode, observable at lower EV (i.e., low P and high v), is replaced by the 'keyhole' mode when higher EV (i.e., high P and low v) are used. The criticism that this method receives is such tracks do not generate molten pools in the exact thermal conditions present in the process, as they are formed without the influence of lateral passes.

The molten pools present in the last layer of the material can be evaluated [32, 33] to compensate for the described limitation of the single-track method, obtaining a more representative description of the process under both the statistical (number of measurements) and representative (normal production conditions) points of

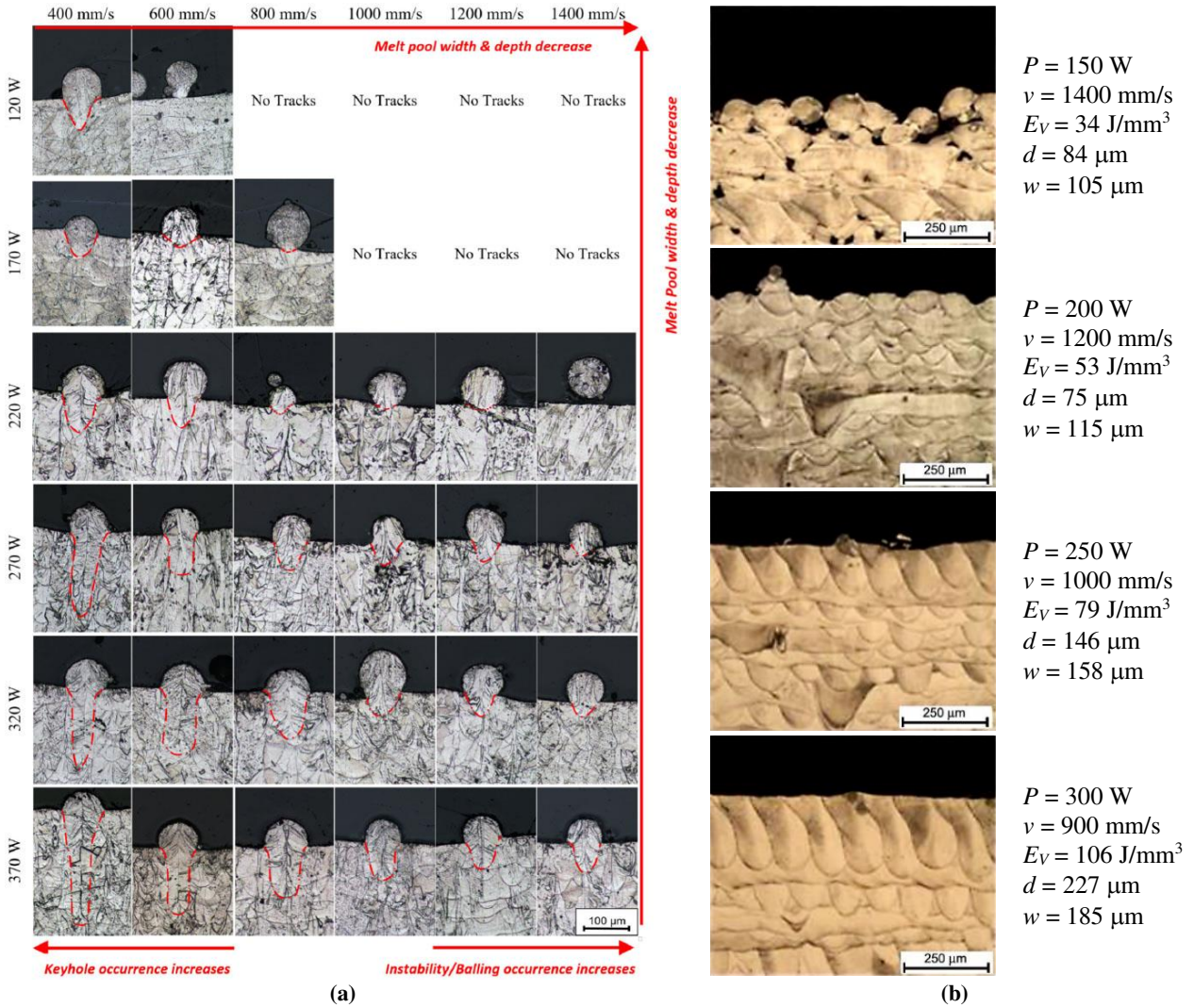

Figure 5. Evaluation of molten pools obtained under different conditions in the LPBF process as seen in metallographic cross-sections in(a) single tracks for Inconel 718 (reactive: Killing #2) [29] and (b) layers finals for the Nb-48Ti alloy (reactive: Kroll) [32].

Copyright © 2022 ISESC

view. In this case, the transient manufacturing conditions will best represent the molten pools obtained in the last layer if preceded by a reasonable number of previous layers on the order of 10 to 20 [27,28, 30]. Figure 5.b illustrates four examples of molten pool measurements from metallographic analyses on the upper layers of a material manufactured by LPBF [32].

When measuring the pools in the last layer, the caveat is that they are overlapped laterally by the subsequent (adjacent) laser scans so that the side that overlapped the previous layer has a full half-width ($w/2$). The overlapping scan has truncated at the other side due to the following laser [17, 31]. The approximation generally considers that the pools would be symmetrical so that twice the half-width ($w/2$) measured on the non-overlapping side represents the total width of the molten pool (w). Additionally, the refusion between adjacent scan tracks in the same layer due to the overlapping ($\%OvR$) can be quantified as Eq. (5) [13, 34]:

$$\%O_vR = 100 \cdot (w - \lambda) / w \quad (5)$$

According to the literature [3-9], inappropriate production parameters can lead to the occurrence of certain defects specific to each melting mode, which reduces the $\%RD$ of products from the LPBF process and, consequently, its 'printability' as described following and as illustrated in Figure 6:

- In conduction mode, if the EV or $\%OvR$ is not high enough, irregularly shaped porosities can be generated due to lack-of-fusion occurrence and residual unfused particles (balling). In this mode, penetration into the previously deposited layer only occurs at a small fraction of the height.
- In 'keyhole' mode, the maximum temperature of the molten pool can exceed the boiling temperature of the alloy or that of some of its lower boiling point constituents, generating steam and unstable collapse of the molten pool and forming so-called porosities of the molten pool "keyhole," present in the deepest portions of the molten pool.

The conduction mode is more desirable since the 'keyhole' mode is considered unstable and produces undesirable porosities in products obtained by AM processes using energy beams. This demonstrates the importance of understanding what conditions prevail to favor the quality control of LPBF products.

2.2. Dynamics of liquid metal in the molten pool

The liquid metal flows within the molten pool, as exemplified in Figs. 4.b and 6 impact crystal growth and the formation of new grains in LPBF [35]. Such flow is composed of the buoyancy generated by the difference in densities between the bottom and top part of the pool and the Marangoni effect [36], which is a convection

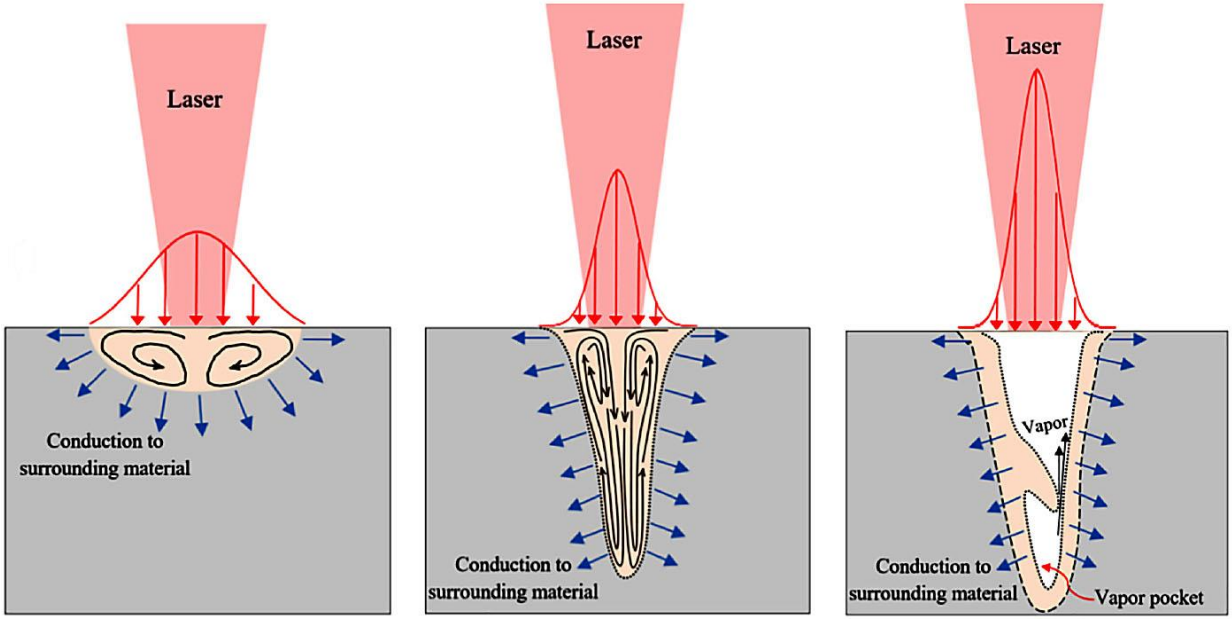

Figure 6. Typical melt pool formation mechanisms of the LPBF process are a) conduction mode and b) 'Keyhole' mode - an example of 'Keyhole' porosity formation [29].

Copyright © 2022 ISESC

phenomenon in which a fluid is driven to move from the regions from low surface tension (γ) to areas of high surface tension, by a Marangoni tension (τ_M) [5, 19]. The high-temperature gradient (G), present in the LPBF process, induces convective buoyancy flows due to the variation in the density of the liquid pool and convective Marangoni flows associated with the variation in surface tension (γ), with such flows being partially limited by the viscosity of the molten pool fluid (η). In general, Marangoni flows are more relevant to LPBF, and Siao and Wen [19] found that the geometry of the molten pool, obtained in simulations of the Marangoni effect, was very similar to that observed in LPBF with AISI 316L steel. Therefore, two movement scenarios in the molten pool may arise depending on the surface tension values, as illustrated in Figure 7.

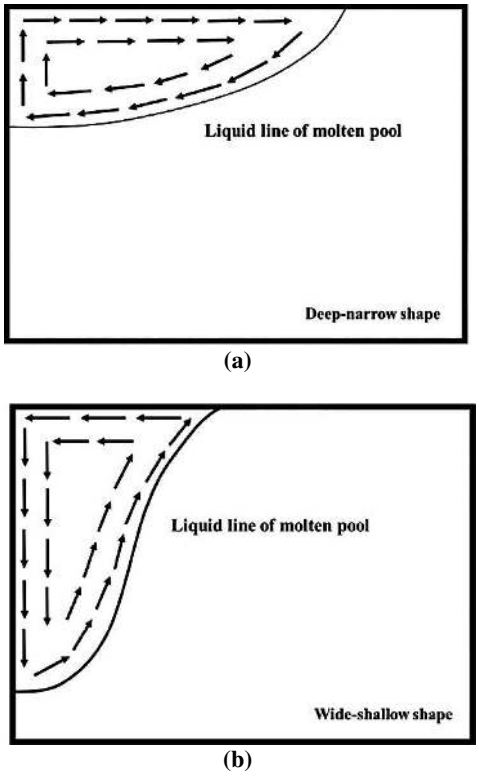

Figure 7. Schematic representation of the flow driven by the Marangoni's effect inside the molten pool with a surface tension: (a) negative and (b) positive [19].

2.3. Molten Pool Boundary

The molten pool boundaries are well defined, as can be seen in metallographies of products obtained by the LPBF, as illustrated in Fig. 5. However, the details of the local interfacial structure at the melt line, including the segregation of alloy solutes, are still unclear. Roehling et al. [23] found that the interface between a track fused by passing a laser over a solid bimetallic substrate (Ti-20Nb and Ti-50Nb) begins as a planar growth front, quickly transforming into cellular growth, with the presence of segregations, as illustrated in Figure 8.

Suppose the structure formed within the weld pool is cellular. In that case, the edge of the molten pool may be formed by a thin region without cellular microstructures and containing segregations due to the decrease in the local cooling rate. This condition was documented in the work of Sato et al. [37] for AISI 316L stainless steel produced by LPBF, whose molten pool edges were observed using scanning electron microscopy (SEM) and transmission electron microscopy (TEM). Some of the results of which are presented in Figure 9.

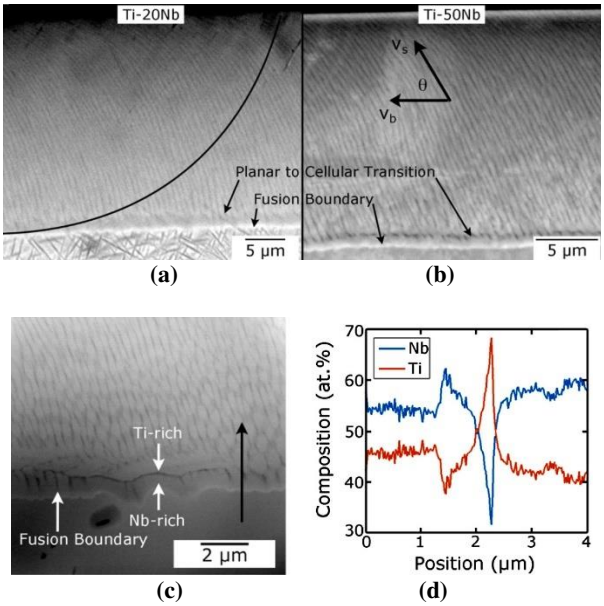

Figure 8. Results of the longitudinal sections analysis in the molten pool boundaries of LPBF products: (a) SEM-BEI for Ti-20Nb alloy and (b) for Ti-50Nb alloy (V_b and V_s are the directions of the laser beam and solidification, respectively); (c) detail of the molten pool of the Ti-50Nb alloy and (d) variation of the chemical composition according to SEM-EDS [23].

However, despite the different conditions present at the edges of the molten pools, both in terms of microstructural formation [23] and segregation [37], the edges of the melting pools do not impede microstructural continuity and surprisingly, not even the alteration of the lattice parameters [38]. It is customary to observe grains passing along the entire structure and causing relevant effects on the behavior and properties of materials produced by the LPBF process [37-40].

Copyright © 2022 ISESC

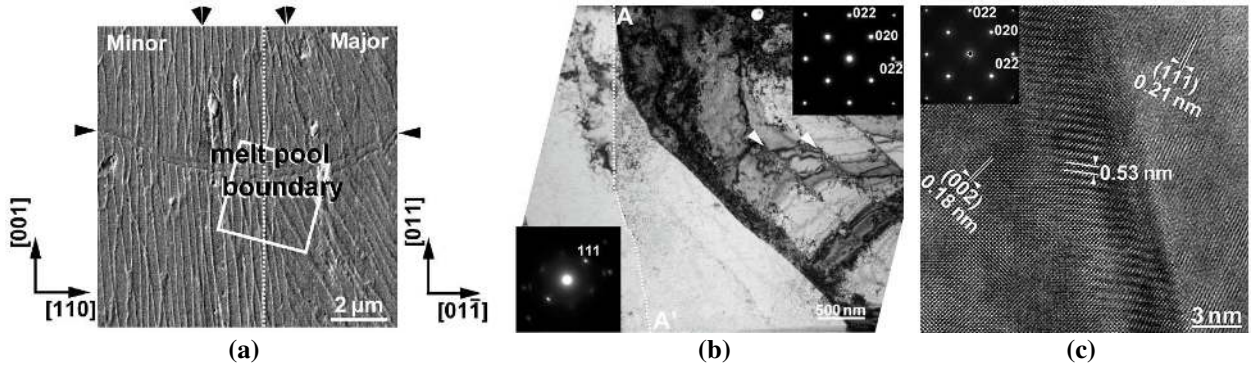

(a) **(b)** **(c)**

Figure 9. Analysis of the edges of the molten pools of an AISI 316L stainless steel part produced by LPBF: (a) SEM-SEI (molten pool front plane); (b) TEM-BF (BF) and corresponding electron diffraction patterns (the vertical line A-A′ defines a molten pool boundary, and the arrows indicate cellular microstructures); (c) HR-TEM in a lamellar boundary illustrating interplanar distances variation [37].

2.4. Effect of molten pool geometry on the structure

As a result of the high cooling rates ($\dot{T}$) and thermal gradients (G) typical of AM by LPBF, solidification in this process occurs through the formation of columnar or dendritic cellular structures [41-43]. The change in the profile of the incident laser beam, from circular Gaussian to elliptical or even with homogeneous distribution ('top hat' type), induces a change in the morphology of the grains formed in the LPBF process. Simulations suggest that the increase in convective flows (see item 2.2), associated with the change in the type of laser energy distribution, induces dendritic fragmentation [35], giving preference to the nucleation of an equiaxed grain structure [23].

Furthermore, the speed imposed on the solidification process restricts the nucleation of crystals in the molten pool, favoring solidification and growth from the present crystalline substrate formed by the fusion of the previous layers, as illustrated in Figure 10.a. Such epitaxial growth probably occurs in the homoepitaxial mode, as defined by Markov [44], with the surfaces involved presenting similar chemical potentials, but network parameters differentiated by thermal expansion associated with the large temperature gradient present at the solid-liquid interface, as shown in Fig. 9.

The particular solidification conditions of AM by LPBF impose a predominant solidification direction in this process as the one that best reconciles the directions of maximum heat extraction ($\partial Q/\partial t$), or the temperature gradient (G), with the direction of preferential crystalline growth ($D_{<uvw>}$), for example, <100> in CCC and CFC metals [20, 45, 46]. The relationship between the crystalline orientation of the manufactured product and its final geometry will depend on the reconciliation between its dimensions and shapes with the directions of maximum heat extraction from the process, epitaxial growth of the crystalline structure of the metal used and the competition in growth between the different crystals formed with possible variation in heat extraction, as illustrated in Figure 10.b. Therefore, different molten pool geometries and, consequently, other forms of heat extraction will induce different epitaxial and competitive growth dynamics of the structure, as illustrated in Figures 10.b to 10.d and in the microscopies shown in Figure 11, as obtained by the present authors.

Wang and Zou [47] summarize the type of microstructure formed by the conduction mode, with d/w < 1.0 as composed of equiaxed grains tending to be more oriented than those formed in the molten pools in 'keyhole' mode, in which d/w > 1.5, and in both cases epitaxial growth is the mechanism present [23].

2.5. Effect of overlapping molten pools

The grain structure in LPBF products is affected by a single scanning pass and successive tracks or layers [7, 20]. Considering the lateral effect of trail succession, competitive growth in the overlapping region, far from the middle of the molten pool, results in cellular structures [48]. This region can be observed on the 'dark' side (left) of the 'keyhole' pools (E_V = 79 and 106 J/mm^3) shown in Fig. 5.b. In the middle of the molten pool, grain growth is dominated by the [001] direction, which is responsible for developing elongated grains due to successive layers or tracks, as shown in Figure 12. This condition allows the possibility of programming the material structure through directional solidification by synergy between the various scanning tracks used in the FLP-L process, as suggested by Luo et al. [49].

Copyright © 2022 ISESC

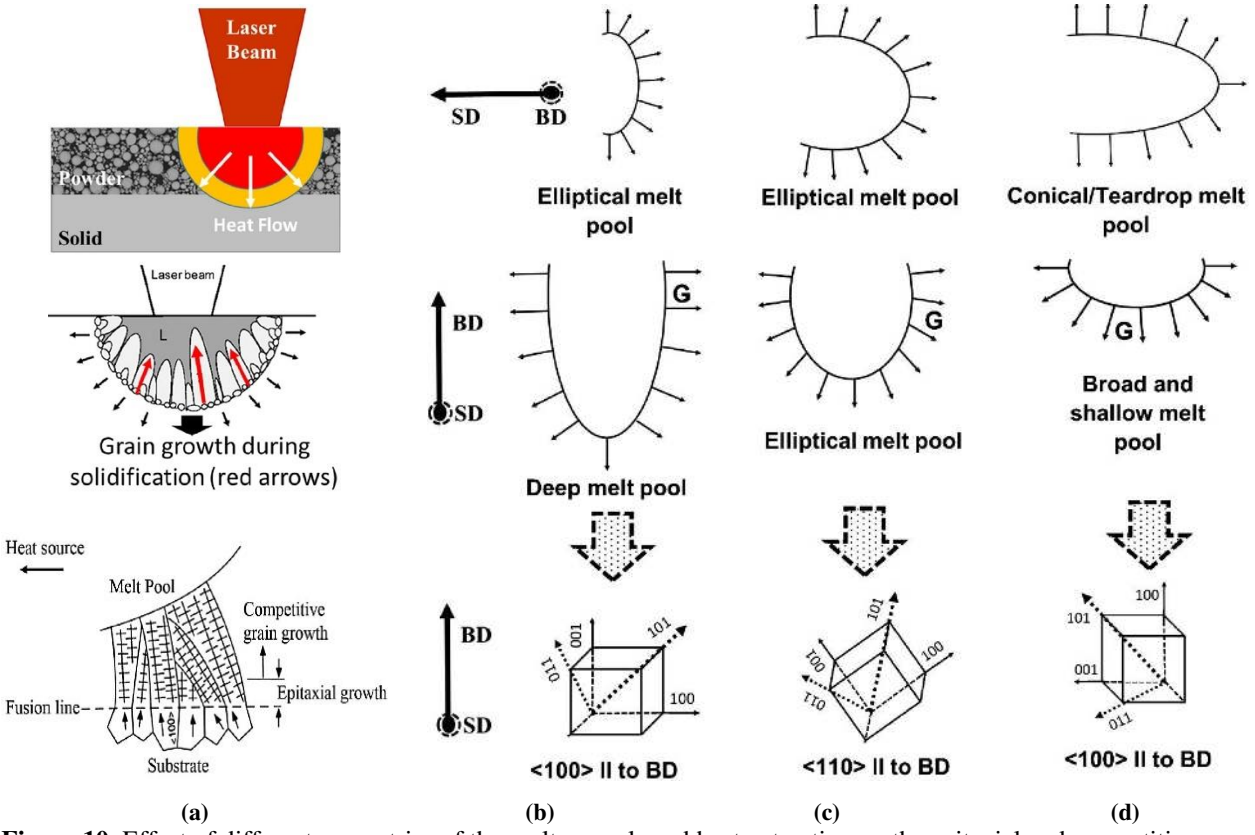

Figure 10. Effect of different geometries of the molten pools and heat extraction on the epitaxial and competitive growth of the structure in AM by LPBL: (a) local formation at the edge of the molten pool [9, 45] and (b) to (d) crystallographic growth domain regions as a function of reconciling the temperature gradient (G), with the preferred crystal growth direction (D<uvw>) [46].

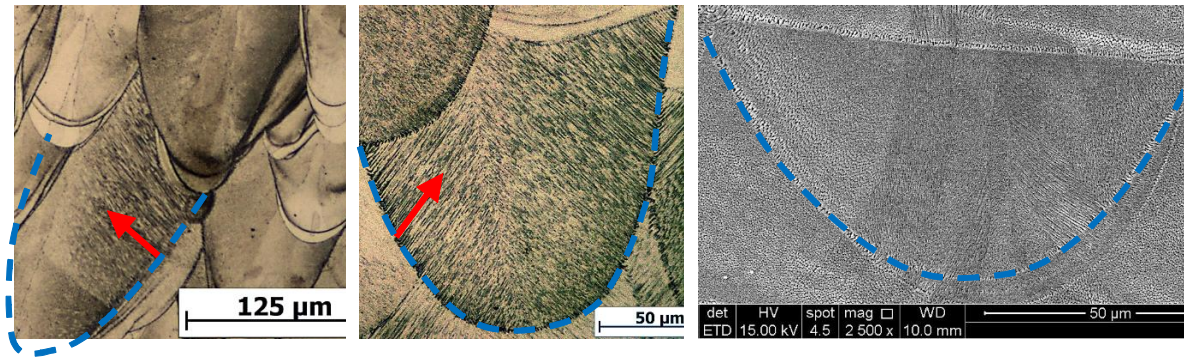

Figure 11. Metallographic records of an Nb-48Ti alloy produced by FLP-L illustrating the effect of different geometries of the molten pools and heat extraction on the epitaxial and competitive growth of the structure in AM by FLP-L: (a) deep molten pool with lateral growth, (b) elliptical molten pool showing diagonal growth and (c) shallow molten pool showing vertical growth [17, 32, 39, 40].

Although predictions of molten pool dimensions (width and depth) in literature simulations agree well with general metallographic measurements (see item 2.1), detailing the exact molten pool geometries is more challenging because of superposition (*%OvR*) between the pools, especially with higher *%OvR* values [50].

Copyright © 2022 ISESC

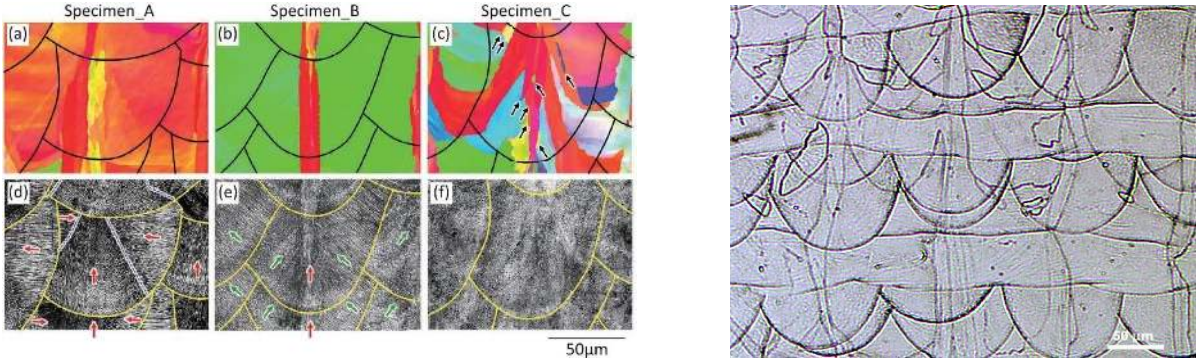

(a) **(b)**

Figure 12. Presence of columnar grains aligned in the [001] direction as seen in LPBF: (a) structures and inverse pole figures obtained with different processing conditions of AISI 316L steel [33] (low, medium and high velocities for specimen A, B, and C, respectively) and (b) metallography (Kroll etching) illustrating a columnar grain structure at the bottom of molten pools for the Nb-48Ti alloy [40].

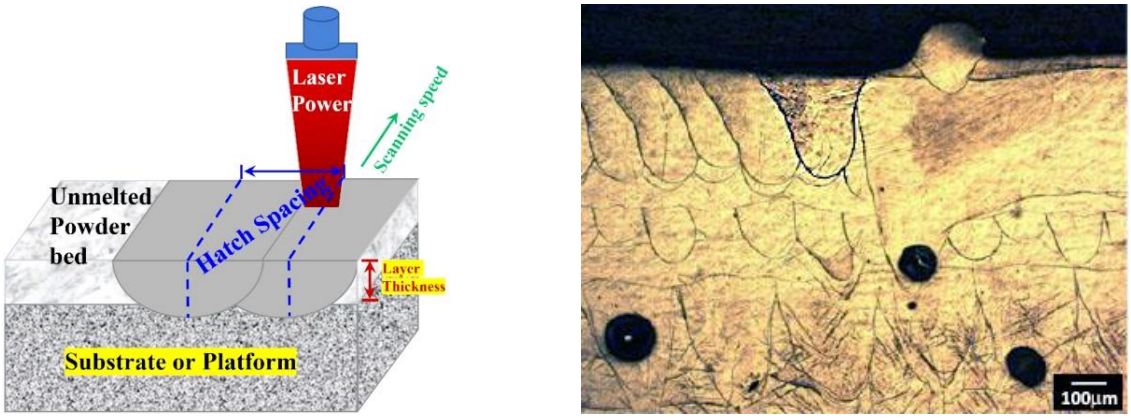

(a) **(b)**

Figure 13. Asymmetric formation of molten pools in the LPBF process: (a) illustrativ7e scheme of the superimposition of a new track (2) on an already deposited track (1) and the other on the powder bed in which *%OvR* ≈ 50% [52]; (b) example of the last molten pool (red arrow) deposited in the upper layer of a Ti-13Nb-13Zr alloy that does not have symmetry along a // BD axis (blue dotted line), the porosities present are of the 'keyhole' type [53].

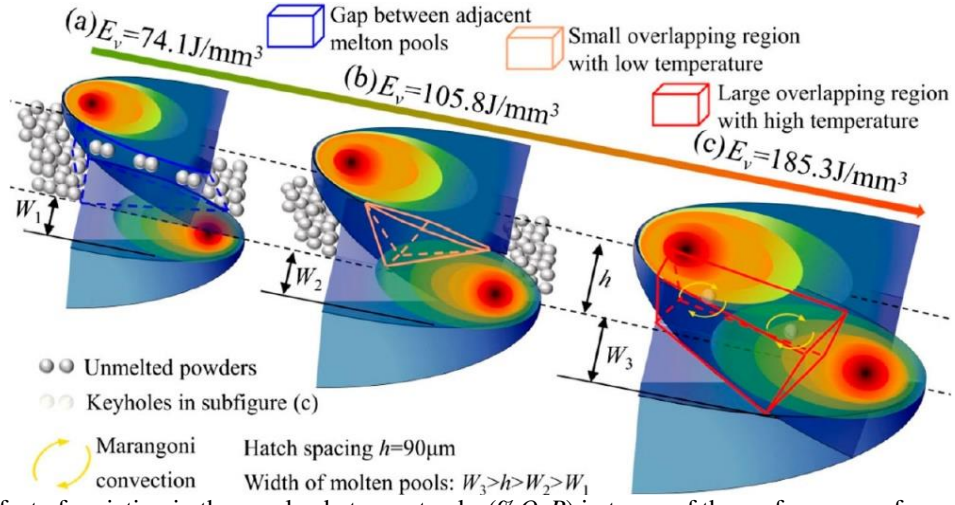

Figure 14. Effect of variation in the overlap between tracks (*%OvR*) in terms of the performance of a product obtained by the LPBF process [51].

Copyright © 2022 ISESC

Molten pools form under asymmetric conditions, as one side of the molten pool covers a particular portion of solid material, proportional to the *%OvR* value, as illustrated in Figure 13.a. The solid portion has a thermal conductivity about 100 times greater than the loose powder [31], causing one side of the molten pool to have a more significant thermal gradient [48], leading to more excellent fusion and penetration of the molten pool on the side with more considerable overlap, which leads to generating asymmetrical pools, such as the one illustrated in Figure 13.b.

Zhang et al. [51] discuss the importance of the effect of overlap on the performance of a nickel superalloy (Invar 36) in terms of producing defects due to lack of fusion or unfused particles with low *%OvR*, more homogeneous structures with an intermediate overlap or the possible occurrence of 'keyhole' defects, when there is an exaggerated overlap inducing 'keyhole' fusion mode conditions. Figure 15 shows how the overlapping can vary in function of volumetric energy (E_v), generating or not superimposed regions with high temperature and Marangoni fluxes [51].

The most appropriate overlap between the molten pools will depend on the objective and properties achieved with the LPBF process product. Sun et al. [20], as well as Andreau et al. [31], describe the need to reconcile molten pool geometries in lateral (along TD) and vertical (along BD) overlap so that thermal gradients (G) are aligned with the preferential crystalline growth directions ($D_{<uvw>}$) to stimulate certain types of crystalline texture.

Figure 15 illustrates the final effect of the variation in the distance between passes (λ) on the solidification and microstructural formation of products by the LPBF process. Note that it is possible to define the structure obtained between planar, columnar, cellular, and equiaxed by adjusting the distance between the tracks (i.e. *%OvR*) without necessarily changing the power (P) and speed (v) conditions of the process and without leaving the “processing window”.

In the same line, Luo et al. [49] present similar results of controlling properties through the geometry of the molten pools and their positioning, inducing {100] texture or not depending on the processing conditions for

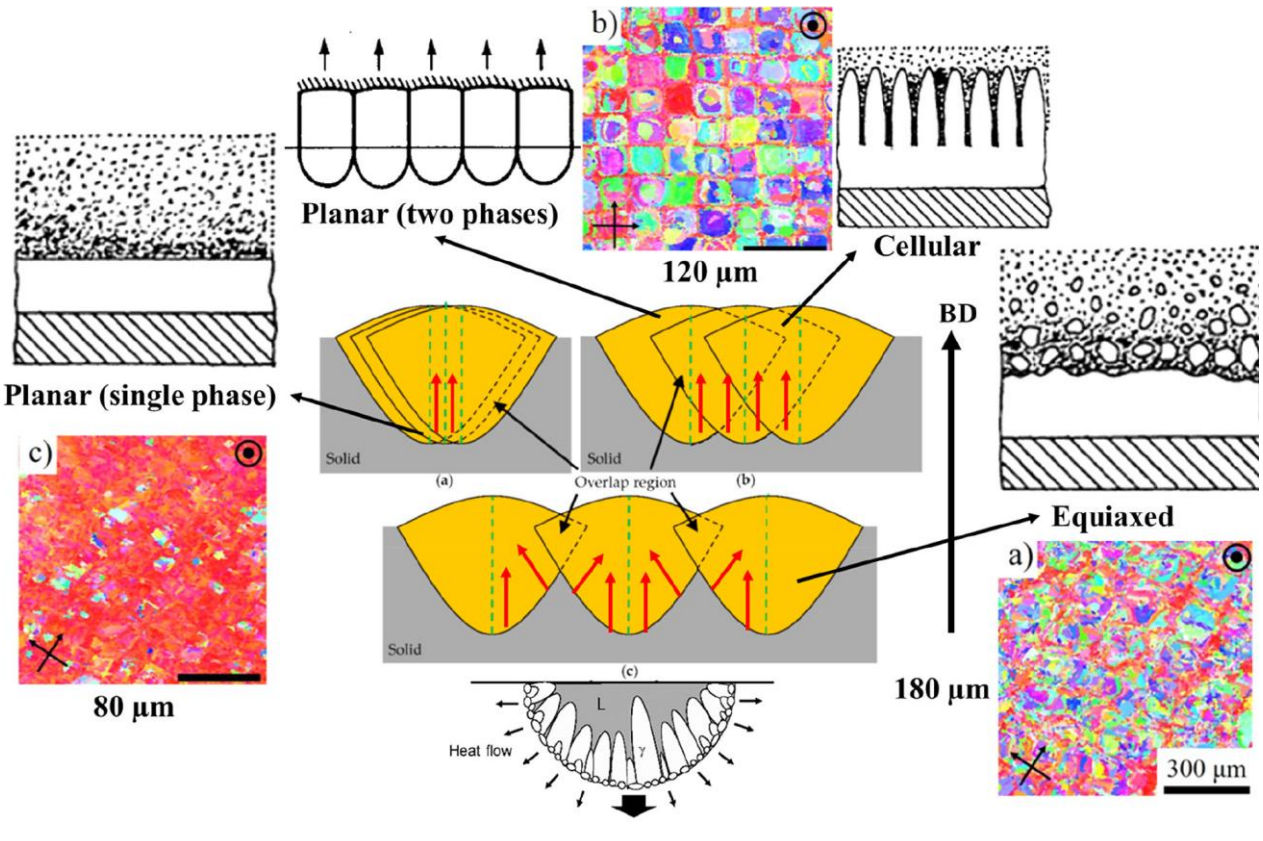

Figure 15. Impact of the spacing between passes (λ) and consequently the overlap (*%OvR*) on the solidification and microstructural definition in NiTi alloys obtained by LPBF [21].

Copyright © 2022 ISESC

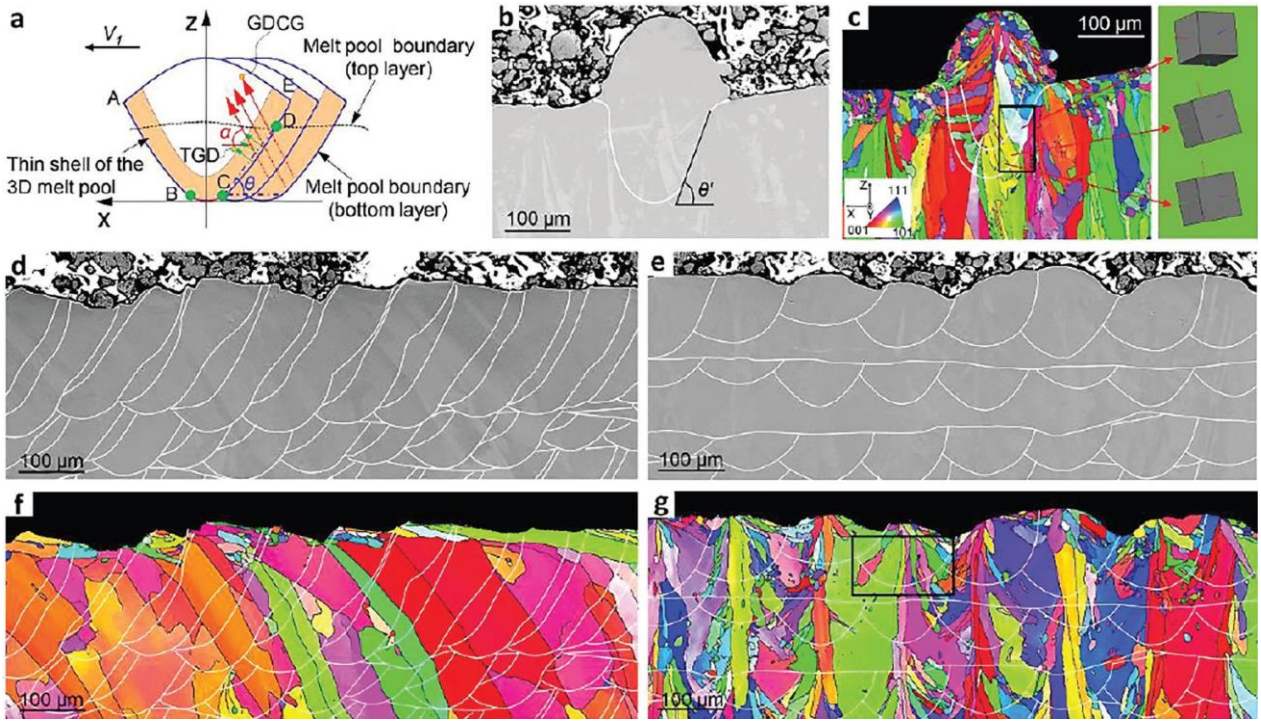

Figure 16. Possible use of the geometry of the pools and the amount of overlap to obtain differentiated structures as presented by their respective orientation maps obtained by EBSD for Ti-Nb-Zr-Ta alloys processed by LPBF [48].

a Ti-Nb-Zr-Ta biomedical alloy, as summarized in Figure 16.

3. Conclusions

The formation, geometry, and overlaps of molten pools in the AM process by LPBF are a subject of continuous interest in the literature because, as presented in this work, the literature indicates that controlling the formation and dynamics of molten pools serves to not only maintain quality to obtain acceptable density values in the parts but also establish and regulate the properties of the product through microstructural control. Based on the literature information and guidelines presented in this work, detailed measurements can be made to describe LPBF products. An example of such an approach is presented and discussed for Nb-48Ti elsehere [54].

Acknowledgments

The authors acknowledge the Companhia Brasileira de Metalurgia e Mineração (CBMM), Fundação de Amparo à Pesquisa do Estado de São Paulo (FAPESP) for their financial support (process number 2016/50199-6), Instituto de Pesquisas Tecnológicas (IPT), and Instituto Senai de Inovação em Sistemas de Manufatura e Processamento a Laser. F. J. G. Landgraf thanks to the support of the CNPq (grant 308991/2022-2).

References

1 Meyers M. A., and Chawla K. K. “Mechanical behavior of materials”. 2nd ed. Cambridge: Cambridge University Press; 2009.

2 Callister W. D. Jr, and Rethwisch, D. G. “Fundamentals of materials science and engineering: an integrated approach”. 5th ed. Versailles: John Wiley & Sons; 2019.

3 Gibson, I., Rosen, D. W., Stucker, B. “Additive Manufacturing Technologies: Rapid Prototyping to Direct Digital Manufacturing”. New York (USA): Springer; 2010.

4 Brandt, M. “Laser Additive Manufacturing: Materials, Design, Technologies, and Applications”. Duxford (UK): Woodhead Publishing. 2017.

5 Khairallah, S.A., Anderson, A.T., Rubenchik, A., King, W.E. “Laser powder-bed fusion additive manufacturing: Physics of complex

Copyright © 2022 ISESC

melt flow and formation mechanisms of pores, spatter, and denudation zones". Acta Materialia. 2016; 108: p.36-45. https://doi.org/10.1016/j.actamat.2016.02.014.

6 Yadroitsev, I., Yadroitsava, I., Plessis, A.D., MacDonald, E. "Fundamentals of Laser Powder Bed Fusion of Metals". Amsterdam (Netherlands): Elsevier; 2021.

7 Mostafaei, A., Ghiaasiaan, R., Ho, I.T., Strayer, S., Chang, K.C., Shamsaei, N. et al. "Additive Manufacturing of Nickel-based superalloys: a state-of-the-art review on process-structure-defect-property relationship". Progress in Materials Science. 2023; 136 (101108): p.1-180. https://doi.org/10.1016/j.pmatsci.2023.101108.

8 Bontha, S., Klingbeil, N.W., Kobryn, P.A., Fraser, H.L. "Thermal process maps for predicting solidification microstructure in laser fabrication of thin-wall structures". Journal of Materials Processing Technology. 2006;178(1-3):135-142. http://dx.doi.org/10.1016/j.jmatprotec.2006.03.155.

9 DebRoy, T., Wei, H.L., Zuback, J.S., Mukherjee, T., Elmer, J.W., Milewski, J.O., et al. "Additive manufacturing of metallic components-process, structure, and properties". Progress in Materials Science. 2018; 92: p.112-224. https://doi.org/10.1016/j.ijmachtools.2014.09.010.

10 Yin, J., Peng, G., Chen, C., Yang, J., Zhu, H., Ke, L., et al. "Thermal behavior and grain growth orientation during selective laser melting of Ti-6Al-4V alloy". Journal of Materials Processing Technology. 2018; 260:57-65. http://dx.doi.org/10.1016/j.jmatprotec.2018.04.035..

11 Rasch, M., Heberle, J., Dechet, M.A., Bartels, D., Gotterbarm, M.R., Klein, L., et al. "Grain structure evolution of Al-Cu alloys in powder bed fusion with laser beam for excellent mechanical properties". Materials. 2020;13(82):1-22. http://dx.doi.org/10.3390/ma13010082.

12 Wu, Z. D., 2021. "Investigation and Mitigation of Powder Anomalies Induced Porosity in Powder Bed Additive Manufacturing", Ph.D. thesis, Carnegie Mellon University, Pittsburgh, PA (USA).

13 Malekipour, E., El-Mounayri, H. "Common defects and contributing parameters in powder bed fusion AM process and their classification for online monitoring and control: a review". Int J Adv Manuf Technol. 2018; 95: p.527–550. https://doi.org/10.1007/s00170-017-1172-6.

14 Sun, S. H, Hagihara, K., Ishimoto, T., Suganuma, R., Xue, Y. F., Nakano, T. "Comparison of microstructure, crystallographic texture, and mechanical properties in Ti–15Mo–5Zr–3Al alloys fabricated via electron and laser beam powder bed fusion technologies". Additive Manufacturing, Volume 47, 2021, 102329, ISSN 2214-8604, https://doi.org/10.1016/j.addma.2021.102329.

15 Rai, R., Elmer, J. W., Palmer, T. A., DebRoy, T. "Heat transfer and fluid flow during keyhole mode laser welding of tantalum, Ti–6Al–4V, 304L stainless steel and vanadium". Journal of Physics D: Applied Physics. Volume 40, Number 18, 2007, Pages 5753–5766. ISSN 0022-3727, http://dx.doi.org/10.1088/0022-3727/40/18/037 .

16 Vrancken, B. "Study of residual stresses in selective laser melting", Ph.D. thesis, Heverlee: KU Leuven, Faculty of Engineering Science; 2016 [cited 2021 Ago 2]. Available from: https://lirias.kuleuven.be/retrieve/391175.

17 Morais, W. A., Hernández, J. S. G., Machado, I. F. e Landgraf, F. J. G. "Study of the molten pool size of a Nb-48Ti alloy produced by laser powder bed fusion additive manufacturing", p. 2493-2504. In: 76º Congresso Anual da ABM - Internacional, São Paulo, 2023. https://doi.org/10.5151/2594-5327-40354.

18 Hagihara, K., Nakano, T. "Control of Anisotropic Crystallographic Texture in Powder Bed Fusion Additive Manufacturing of Metals and Ceramics - A Review". JOM 74, 1760–1773. 2022. https://doi.org/10.1007/s11837-021-04966-7.

19 Siao, Y. H., Wen, C. D. "Examination of molten pool with Marangoni flow and evaporation effect by simulation and

Copyright © 2022 ISESC

experiment in selective laser melting", International Communications in Heat and Mass Transfer, Volume 125, 2021, 105325, ISSN 0735-1933, https://doi.org/10.1016/j.icheatmasstransfer.2021.105325.

20 Sun, S. H., Hagihara, K., Nakano, T. "Effect of scanning strategy on texture formation in Ni-25 at.%Mo alloys fabricated by selective laser melting". Materials and Design. 2018; 140: 307–316. https://doi.org/10.1016/j.matdes.2017.11.060.

21 Saghaian, S. E., Nematollahi, M., Toker, G., Hinojos, A., Moghaddam, N.S., Saedi, S., et al. "Effect of hatch spacing and laser power on microstructure, texture, and thermomechanical properties of laser powder bed fusion (L-PBF) additively manufactured NiTi". Optics & Laser Technology. 2022; 149:1-14. http://dx.doi.org/10.1016/j.optlastec.2021.107680.

22 Morais, W. A., Landgraf, F. J. G. "Crystallographic texture configured by laser powder bed fusion additive manufacturing process: a review and its potential application to adjust mechanical properties of metallic products". Tecnol Metal Mater Min. 2023; 20: e2802, https://doi.org/10.4322/2176-1523.20222802.

23 Roehling, J. D., Perron, A., Fattebert, J.-L., Haxhimali, T., Guss, G., Li, T. T. et al. Rapid Solidification in Bulk Ti-Nb Alloys by Single-Track Laser Melting. JOM 70, 1589–1597 (2018). https://doi.org/10.1007/s11837-018-2920-2.

24 Wang, H., Zou, Y. "Microscale interaction between laser and metal powder in powder-bed additive manufacturing: Conduction mode versus keyhole mode", International Journal of Heat and Mass Transfer, Volume 142, 2019, 118473, ISSN 0017-9310, https://doi.org/10.1016/j.ijheatmasstransfer.2019.118473.

25 Kou, S. "Welding Metallurgy". New Jersey (USA): John Wiley & Sons, Inc; 2003.

26 Markl, M., Lodes, M., Franke, M., Körner, C. "Additive manufacturing using selective electron beam melting". Welding and Cutting 16 (2017) No. 3

27 Thijs, L.; Sistiaga, M. L. M.; Wauthle, R.; Xie, Q.; Kruth, J-P.; Humbeeck, J. V. "Strong morphological and crystallographic texture and resulting yield strength anisotropy in selective laser melted tantalum". Acta Materialia 61, pp. 4657–4668, 2013. https://doi.org/10.1016/j.actamat.2013.04.036.

28 Manvatkar, V.; DebRoy, T. "Spatial variation of melt pool geometry, peak temperature and solidification parameters during laser assisted additive manufacturing process". Materials Science and Technology, 31:8, 924-930, 2015. https://doi.org/10.1179/1743284714Y.0000000701.

29 Balbaa, M., Mekhiel, S., Elbestawi, M., McIsaa, J. "On selective laser melting of Inconel 718: Densification, surface roughness, and residual stresses". Materials and Design. 2020; 193 (2020): 108818. https://doi.org/10.1016/j.matdes.2020.108818.

30 Mukherjee, T. Zhang, W., DebRoy, T. "An improved prediction of residual stresses and distortion in additive manufacturing". Computational Materials Science, Volume 126, 2017, Pages 360-372, ISSN 0927-0256, https://doi.org/10.1016/j.commatsci.2016.10.003.

31 Andreau, O., Koutiri, I., Peyre, P., Penot, J. D., Saintier, N., Pessard, E., et al. "Texture control of 316L parts by modulation of the melt pool morphology in selective laser melting". Journal of Materials Processing Technology. 2019; 264: p. 21-31. https://doi.org/10.1016/j.jmatprotec.2018.08.049.

32 Hernández, J. S. G. "Análises microestruturais e mecânica da liga Ti-53%Nb produzida por fusão seletiva a laser usando pós esféricos e irregulares", Dissertação de Mestrado, Escola Politécnica da Universidade de São Paulo; 2019. https://doi.org/10.11606/D.3.2020.tde-21042020-100214.

33 Ishimoto T, Wu S, Ito Y, Sun SH, Amano H, Nakano T. "Crystallographic orientation control of 316L austenitic stainless steel via selective laser melting". ISIJ International. 2020; 60 (8):1758-1764. http://dx.doi.org/10.2355/isijinternational.ISIJINT-2019-744.

Copyright © 2022 ISESC

34 Di, W., Yongqiang, Y., Xubin, S., Yonghua, C. "Study on energy input and its influences on single-track, multi-track, and multi-layer in SLM". Int J Adv Manuf Technol. 2012; 58 (2): p. 1189–1199. https://doi.org/10.1007/s00170-011-3443-y.

35 Yu Y, Wang L, Zhou J, Li H, Li Y, Yan W, Lin F. "Impact of fluid flow on the dendrite growth and the formation of new grains in additive manufacturing", Additive Manufacturing, Volume 55, 2022, 102832, https://doi.org/10.1016/j.addma.2022.102832.

36 Gong, M., Zhang, S., Lu, Y., Wang, D., Gao, M. "Effects of laser power on texture evolution and mechanical properties of laser-arc hybrid additive manufacturing", Additive Manufacturing, Volume 46, 2021, 102201, https://doi.org/10.1016/j.addma.2021.102201.

37 Sato, K., Takagi, S., Ichikawa, S., Ishimoto, T., Nakano, T. "Microstructure and Solute Segregation around the Melt-Pool Boundary of Orientation-Controlled 316L Austenitic Stainless Steel Produced by Laser Powder Bed Fusion". Materials 2023, 16, 218. https://doi.org/10.3390/ma16010218.

38 Sun, F., Adachi, Y., Sato, K., Ishimoto T., Nakano, T., Koizumi, Y. Quantitative revealing the solute segregation behavior at melt pool boundary in additively anufactured stainless steel using a novel processing method for precise positioning by HAADF-STEM. Materials Characterization, Volume 217, 2024, 114435. https://doi.org/10.1016/j.matchar.2024.114435.

39 Morais, W. A., Falcão, R. B., Boccalini Jr, M., Landgraf, F. J. G. "Fatigue behaviour of additive manufactured Nb-48Ti alloy parts from powders produced by Plasma Atomization (PA) and Hydride-Dehydride (HDH) process". Engineering Failure Analysis, Volume 156, 2024, 107762, https://doi.org/10.1016/j.engfailanal.2023.107762.

40 Morais, W. A., Landgraf, F. J. G. "Correlation between surface and processing parameters of an Nb-48Ti alloy produced by laser powder bed fusion additive manufacturing". Tecnol Metal Mater Min. 2024; 21: e2959, http://dx.doi.org/10.4322/2176-1523.20242959.

41 Sinha, A. K.; Physical Metallurgy Handbook. 1st edition, New York: McGraw-Hill books, 2003.

42 Müller, A. "Solidificação e análise térmica dos metais". 1ª edição, Porto Alegre: Editora UFRGS, 2002.

43 Fredriksson, H., Åkerlind, U. "Solidification and Crystallization Processing in Metals and Alloys". 1st Editon. West Sussex (UK): John Wiley & Sons, 2012.

44 Markov, I. V. Crystal Growth for Beginners. Singapore: World Scientific. 1995.

45 Zhang, X.; Yocom, C.; Mao, B.; Liao, Y. "Microstructure evolution during selective laser melting of metallic materials: A review". J. Laser Appl. 31, 031201, 2019, https://doi.org.10.2351/1.508520.

46 Jadhav, S.D., Dadbakhsh, S., Goossens, L., Kruth, J-P. Van Humbeeck, J., Vanmeensel, K. "Influence of selective laser melting process parameters on texture evolution in pure copper". Journal of Materials Processing Technology, Volume 270, 2019, Pages 47-58, ISSN 0924-0136, https://doi.org/10.1016/j.jmatprotec.2019.02.022.

47 Wang, H., Zou, Y. "Microscale interaction between laser and metal powder in powder-bed additive manufacturing: Conduction mode versus keyhole mode", International Journal of Heat and Mass Transfer, Volume 142, 2019, 118473, ISSN 0017-9310, https://doi.org/10.1016/j.ijheatmasstransfer.2019.118473.

48 Yang, J., Li, F., Pan, A., Yang, H., Zhao, C., Huang, W., Wang, Z., Zeng, X., Zhang, X. "Microstructure and grain growth direction of SRR99 single-crystal superalloy by selective laser melting", Journal of Alloys and Compounds, Volume 808, 2019, 151740, ISSN 0925-8388, https://doi.org/10.1016/j.jallcom.2019.151740.

49 Luo, X., Song, T., Gebert, A., Neufeld, K., Kaban, l., Ma, H., W.Cai, H.Lu, Li, D., Li, N., Li, Y., Yang, C., 2023. "Programming crystallographic orientation in additive manufactured beta-type Titanium alloy". Adv. Sci., 2302884. https://doi.org/10.1002/advs.202302884.

Copyright © 2022 ISESC

50 Amin, A., Li, Y., Lu, Y., Xie, X., Mojumder, S., Gan, Z., Wagner, G., Liu, W. K. "Physics Guided Heat Source for Quantitative Prediction of the Laser Track Measurements of IN718 in 2022 NIST AM Benchmark Test". Research Square; 2023. https://doi.org/10.21203/rs.3.rs-2570334/v1.

51 Zhang, C., Zhou, Y., Wei, K., Yang, Q., Zhou, J., Zhou, H., Zhang X., Yang, X. (2023) "High cycle fatigue behaviour of Invar 36 alloy fabricated by laser powder bed fusion". Virtual and Physical Prototyping, 18:1, https://doi.org/10.1080/17452759.2023.2190901.

52 Subramanian S, Mohanty S, Prashanth KG. "Effect of process parameters on the properties of β-Ti-Nb-based alloys fabricated by selective laser melting: A review". Materials Today: Proceedings. 2023. https://doi.org/10.1016/j.matpr.2023.03.461.

53 Guimarães Jr., J. M. "Estudo microestrutural da liga Ti-13%Nb-13%Zr produzida por fusão em leito de pó a laser com pós esféricos e irregulares". Doctoral qualification, Escola Politécnica da Universidade de São Paulo; 2023.

54 Morais WA, Landgraf FJG. Analysis of the molten pool present in the Nb-48Ti alloy during its processing by laser powder bed fusion.. In: 77º Congresso Anual da ABM - Internacional, São Paulo, 2024. ISSN: 2594-5327, https://doi.org/10.5151/2594-5327-41632.

Copyright © 2022 ISESC